Compact Topological Edge States in Flux-Dressed Graphenelike Photonic Lattices

Gabriel Cáceres-Aravena[1], Milica Nedić,[2] Paloma Vildoso[3], Goran Gligorić[2]

Jovana Petrovic[2], Aleksandra Maluckov[2], and Rodrigo A. Vicencio[3]

[1]*Institute of Physics, University of Rostock, Rostock 18051, Germany*

[2]*Vinča Institute of Nuclear Sciences, National Institute of the Republic of Serbia, University of Belgrade,*
P.O.B. 522, Belgrade 11001, Serbia

[3]*Departamento de Física and Millenium Institute for Research in Optics–MIRO,*
Facultad de Ciencias Físicas y Matemáticas, Universidad de Chile, Santiago 8370448, Chile

Flat band lattice systems promote the appearance of perfectly compact bulk states, whereas topology favors edge localization. In this work, we report the existence of compact topological edge states on flux-dressed photonic graphene ribbons. We found that robust localization is achieved through a synergy of Aharonov-Bohm caging and topological protection mechanisms. The topological nontriviality of the compact edge states is characterized through both theoretical derivations and experimental observations of an integer Zak phase obtained from the mean chiral displacement. Experiments are performed using direct laser writing of a graphene ribbon photonic lattice having 0 or π effective magnetic fluxes. Mode stability is demonstrated by the exceptional localization of the edge compact mode and its resilience to fabrication tolerances and input phase deviations. Our findings demonstrate the existence of perfectly compact topological edge states, as a concrete and promising example of synergy in between flat band physics and topology.

The quest for materials with superconducting properties at convenient operating temperatures has gained new momentum with the possibility to investigate such materials in affordable optical experiments, notably in photonic lattices [1–5]. Departing from the traditional Bardeen-Cooper-Schrieffer theory, it has been hypothesized that the electron pairing around dispersionless energy bands results in superconductivity with the critical temperature linearly proportional to the electron interaction strength [6]. However, dispersionless flat bands (FBs) could store energy in the modes confined, for example, at edges, surfaces or interfaces, and are therefore highly sensitive to environmental influences and fabrication errors [7–11]. On the other hand, stability can be enhanced by an interplay in between Aharonov-Bohm caging and topological protection, such as that realized in Creutz-like ladders [12–15]. However, k independence of FBs does not permit determination of the topological invariants, neither directly, based on the Berry curvature, nor indirectly, based on analogy with the Su-Schrieffer-Heeger (SSH) model [16,17]. All this makes the design of ultrarobust edge states with a FB spectrum challenging.

In response to this challenge, we design a graphenelike photonic ribbon [18] whose topological properties are controlled by a synthetic flux. The induced transitions between trivial and nontrivial topological phases enable probing of the dispersionless band topology and determination of the topological invariants by standard means: mean chiral displacement (MCD) [19–21], two-band

SSH-based graphical method, and numerical projector method [17,22,23]. While a range of fluxes drives the system into a topologically nontrivial phase, a particular flux value $\Phi = \pi$ yields destructive interference and a fully flat band spectrum. The corresponding edge modes are ultraprotected by the synergy of Aharonov-Bohm (AB) and topological effects. We use the femtosecond (fs) laser writing technique [24] to fabricate several quasi-1D graphene ribbon lattices in armchair configuration [18,25,26]. The π flux is implemented by inserting tuned S and P waveguides in a specific sequence through the lattice. By determining the MCD from the experimental data, we confirm the nontriviality of the central bands and the topological origin of the respective edge modes. We experimentally excite these zero edge states and demonstrate their robustness to phase variations and fabrication tolerances. To the best of our knowledge, this is the first complete experimental evidence of an ultrarobust and perfectly compact topologically nontrivial edge state in one-dimensional lattices.

We start by presenting a method for probing the topology of a lattice considering an artificial flux. We do this on a model of a graphenelike ribbon in the armchair configuration, as the one sketched in Fig. 1(a). In the absence of flux, the underlying lattice structure is characterized by bipartite and top-bottom symmetries, in which each unit cell consists of six linearly coupled sites. Evolution of the complex optical field $\psi_n = (A_n B_n C_n D_n E_n F_n)^T$, with $n = 1, \ldots, N$, and N the number of unit cells,
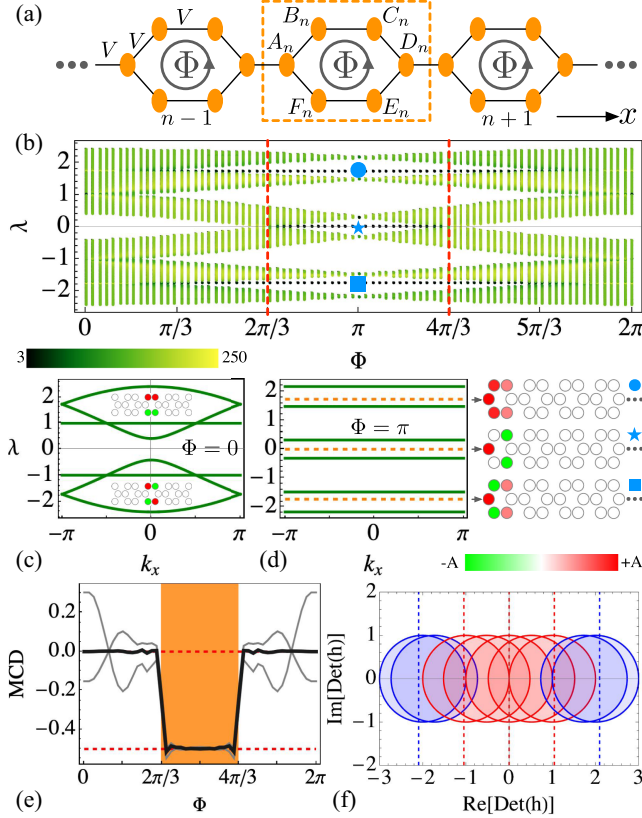
FIG. 1. (a) Graphenelike ribbon lattice with flux Φ. (b) Band spectrum of a finite lattice ($N = 50$) as a function of flux Φ. Color indicates the respective participation ratio. (c) and (d) The band spectra λ vs k_x for fluxes $\Phi = 0$ and π, respectively. Profiles in (d) correspond to edge states at dashed lines. (e) Mean chiral displacement (MCD) as a function of Φ (black solid line). Gray lines show MCD for single A, C, E site excitations. (f) $\text{Det}(h) = -\cos k_x + 2\cos(\Phi/2) + i\sin k_x$ in the complex plane. In (b)–(e) $V = 1$.

is governed by a set of linear Schrödinger coupled equations in k_x space:

$$i\frac{d\tilde{\psi}(k_x)}{dz} = \hat{H}(k_x)\tilde{\psi}(k_x). \tag{1}$$

Here, $\tilde{\psi}(k_x)$ is the optical field in k_x-space, k_x the transversal quasimomentum, z the propagation coordinate, and $\hat{H}$ the Bloch Hamiltonian. The presence of flux Φ breaks the top-bottom lattice symmetry and introduces imaginary components into the coupling coefficients:

$$\hat{H} = \begin{pmatrix} 0 & \mu^* & 0 & \nu^* & 0 & \mu \\ \mu & 0 & \mu^* & 0 & 0 & 0 \\ 0 & \mu & 0 & \mu^* & 0 & 0 \\ \nu & 0 & \mu & 0 & \mu^* & 0 \\ 0 & 0 & 0 & \mu & 0 & \mu^* \\ \mu^* & 0 & 0 & 0 & \mu & 0 \end{pmatrix}, \tag{2}$$

where $\mu = Ve^{i\phi}$ and $\nu = Ve^{ik_x}$ are the complex intra- and intercell coupling coefficients, respectively, and $\phi = \Phi/6$ [27]. $\hat{H}$ possesses chiral symmetry: $\hat{H} = \hat{G}\hat{H}\hat{G} = -\hat{H}$, with $\hat{G}$ as the chirality operator given by $\hat{G} = (\hat{B} + \hat{D} + \hat{F}) - (\hat{A} + \hat{C} + \hat{E})$. ($\hat{A} = \sum_n |A_n\rangle\langle A_n|$ is the sublattice projector operator on A lattice sites, $\hat{B}$ on B site components, etc.)

Now, we compute the eigenvalue spectrum $\{\lambda\}$, representing the propagation constants along the z direction, for a finite lattice with $N = 50$ unit cells. We show our results in Fig. 1(b), where the darker color corresponds to a smaller participation ratio, i.e., stronger localization. In the absence of flux [see Fig. 1(c)] the bipartite ribbon spectrum contains an empty gap around zero, a pair of symmetric flat bands at $\lambda = \pm V$ (with the FB states as insets), and two pairs of dispersive bands [18]. In this case, there are no isolated bands, and the topological invariant is not defined. Interestingly, the introduction of flux Φ preserves the chiral symmetry of the system. Singular FBs are transformed into gapped dispersive bands, and an opening of the two gaps between outer bands hosting a doublet of edge modes each [circles and squares in Figs. 1(b) and 1(d)]. A further increment in flux Φ results in the closing and reopening of the central gap at $\Phi = 2\pi/3$ (dashed vertical line). Here, the creation of a pair of $\lambda = 0$ (zero) edge states is observed [stars in Figs. 1(b) and 1(d)], in analogy with a SSH lattice [29]. These degenerated edge modes decay exponentially from the respective surface and their localization increases as the central band gap increases [27]. The spectrum symmetry dictates the reverse trend as the flux is further increased, closing the gap at $\Phi = 4\pi/3$ (dashed vertical line) and restoring the original topologically trivial lattice properties. Therefore, a continuous modification of flux Φ transforms the lattice topology, leading to the emergence of compact and robust edge states.

For a particular value of flux $\Phi = \pi$, the Aharonov-Bohm effect causes the bands to collapse into flat bands [30], forming a fully flat multiband spectrum [see Figs. 1(b) and 1(d)]. The flatness is associated with degeneration of $6(N-1)$ eigenvalues into 6 flat bands at $\lambda = \pm 2.17, \pm 1.48, \pm 0.31$ V with $N-1$ times degeneration each. In the gaps in between the flat bands, the triplet of double degenerate edge modes continues to exist at $\lambda = 0, \pm\sqrt{3}$ V [horizontal dashed lines and edge mode profiles in Fig. 1(d)]. As a result of destructive interference, all the corresponding edge mode profiles feature zero light power at the connecting lattice sites A or D. This fully prevents state transport and bulk dispersion. Specifically, at $\Phi = \pi$, the zero edge modes are perfectly compact and formed by only three nonzero amplitude sites. These perfectly compact edge states cannot be formed by any FB state superposition [31].

An estimate of bulk topological invariant is mandatory to ascertain the topological nontriviality of the compact edge states. However, topological invariants elude a clear definition in systems with a FB k-independent spectrum.

To resolve this, we tune the synthetic flux and evaluate the invariant (Zak phase in this case), in the k-dependent spectral region, upon which we formally converge to values at $\Phi = \pi$. Zak phase, also known as winding number [17,22], provides information about the winding behavior of the energy bands in the momentum space, distinguishing between different topological lattice phases. Because of the bulk-edge correspondence [32–34], an integer value of Zak phase in units of π is equal to the number of edge-mode pairs within a gap. The nontriviality of the zero edge modes is proven by the MCD calculated as a displacement (in cells units) of the spatial profile from the input position [19]. It is an extension of the mean field displacement (MFD), which is empirically determined as the mean displacement of the center of a propagating wave packet [35–37], to chiral multiband SSH-like lattices [27]. We excite one by one each site inside the central unit cell hosting the eigenstates of the chiral operator: A, C, E or B, D, F, which correspond to the eigenvalues 1 and −1 of the chiral operator, respectively. The MCD is then determined as an average of the three MFDs. The Zak phase of the central ribbon bands is subsequently defined as twice the MCD value. Figure 1(e) shows the dependence of MCD on flux and that the MCD takes values close to −0.5 in the whole nontrivial region: $\Phi \in [2\pi/3, 4\pi/3]$. Thus the MCD can be used as a clear nontriviality parameter in a lattice with multiple FBs.

Reopening and reclosing of the central gap, accompanied by the appearance of zero edge modes, is analogous to what is observed in the SSH model. The bipartite symmetry provides ability to transform $\hat{H}(k)$ of the flux-dressed ribbon lattice into an off-diagonal block SSH-like matrix parametrized by flux Φ [27]. Then, the winding number of the ribbon can be estimated by plotting the determinant of the off-diagonal submatrix h in the complex plane [see Fig. 1(f)] and observing how many times it winds around the origin. The topological phase transition is marked by the zeros of the determinant at $\Phi = 2\pi/3$ and $\Phi = 4\pi/3$. The flux values within these limits render the lattice topologically nontrivial regime. For $\Phi = \pi$, the determinant draws a zero-centered circle reproducing the k_x invariance. An additional confirmation of the zero-mode topological origin is achieved by the projector method [22,23,32]. This method utilizes the band projectors $\hat{P}(k)$ over the $\hat{H}$ eigenvalue basis, as described at Supplemental Material [27]. Based on all these arguments, we conclude that the zero edge modes found in this model are protected by both destructive interference (arising from Aharonov-Bohm caging) and lattice topology. Hence, these states are perfectly localized, compact, and ultrastable stationary solutions.

We provide experimental evidence of the trivial and nontrivial topological properties of a graphene-like ribbon photonic lattice in two experimentally available cases: $\Phi = 0$ and π. Different lattices are fabricated inside an $L = 70$ mm borosilicate glass wafer by direct laser
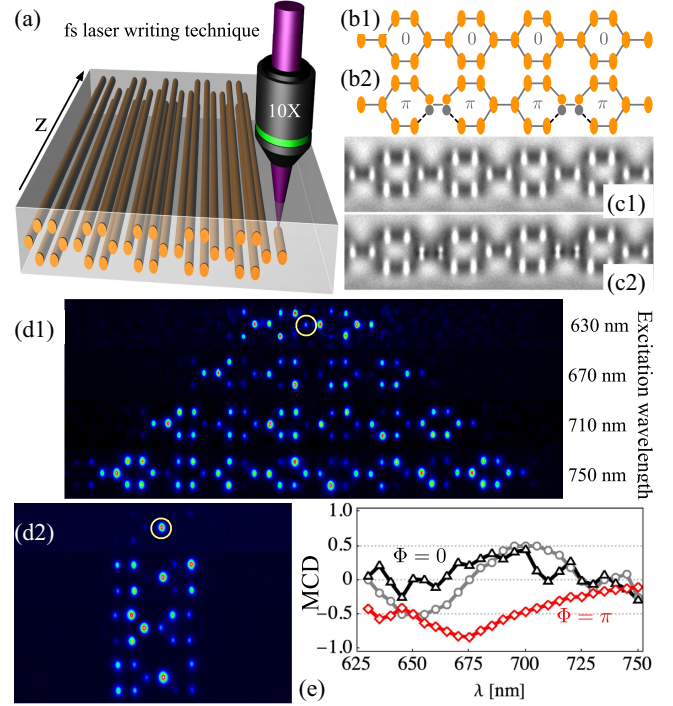

FIG. 2. (a) Illustration of the fs-laser writing technique. (b1) and (b2) S and SP configurations (fluxes denoted in each case). (c1) and (c2) White-light microscope images for fabricated lattices. (d1) and (d2) Output intensities after a D site excitation (yellow circle), on a ribbon with $\Phi = 0$ and $\Phi = \pi$, respectively. Excitation wavelengths of both cases are indicated in (d1). (e) MCD for sites ACE versus wavelength, for trivial (black) and topological (red) lattices. Gray data in (e) show the averaged MCD for CE sites only.

writing [24], as sketched in Fig. 2(a). A lattice composed of S waveguides only [18] [see sketch in Fig. 2(b1) and implementation in Fig. 2(c1)] implies a trivial flux $\Phi = 0$. A nontrivial flux is induced by replacing a set of S waveguides with dipole-like P waveguides at every other hexagon, as shown in Figs. 2(b2) and 2(c2). The presence of P waveguides on a lattice produces the appearance of negative coupling constants and, in this specific case, the effective induction of a flux $\Phi = \pi$ at every closed ring [30]. An effective interaction of S and P modes is achieved by a tuning optimization protocol [38], where their propagation constants are matched at neighboring waveguides around a given wavelength (∼640 nm in our experiments).

First of all, we study bulk transport by exploiting the rather linear dependence of coupling constants on wavelength [15,37]. Different excitation wavelengths effectively describe a different dynamical instant "Vz" [27]; therefore, we capture the transport through the lattice by varying this parameter [27]. These experiments were performed using a supercontinuum (SC) laser beam, in the wavelength range of {630,750} nm, which was tightly focused to excite individual lattice sites. We first excite the trivial lattice at a

bulk D site [Fig. 2(d1)] and observe a ballisticlike transport, similar to discrete diffraction of 1D lattices [37]. In this case, the input excitation does not excite the FB modes and only the dispersive part of the spectrum is activated. The excitation of individual B, C, D, E sites results in a mixture of diffraction and localized energy oscillations at the input ring region [18,27]. A strongly contrasting behavior is observed for a nontrivial flux $\Phi = \pi$, as shown in Fig. 2(d2). For an identical bulk D excitation, the light cannot overcome the flux-induced effective barrier and remains oscillating on a quite reduced area, covering only two lattice rings. This is a result of the AB caging effect in a system with a flat-only linear spectrum [see Fig. 1(d)]. Interestingly, the caging effect is observed for a very broad wavelength range.

For bulk excitation, we compute the MCD from the experimental data by averaging the mean displacements of individual excitations of A, C, and E bulk lattice sites [see Fig. 2(e)], consistently with the lattice chiral symmetry [27]. For $\Phi = 0$ (black data), the MCD oscillates around zero, indicating a zero Zak phase. The light is diffracting strongly through the lattice [Fig. 2(d1)] experiencing inhomogeneities induced by the fabrication process, which slightly randomizes the MCD value. The average of CE sites only (gray data) shows an oscillation around zero, as these sites mainly excite the FBs, with the light oscillating mostly inside a single unit cell [27]. For $\Phi = \pi$, the nontriviality of the lattice becomes evident with MCD values around -0.5 (red data). The MCD is closest to -0.5 around the wavelength of 640 nm, for which the nontriviality condition is fully fulfilled. Therefore, we have dynamically measured the trivial and nontrivial properties of the graphenelike ribbon, which naturally depend on the specific applied flux.

To study the edge excitation, we first excite the site A at the left edge of both lattices. In the trivial $\Phi = 0$ lattice, we observe only transport with the light strongly repelled from the edge [see Fig. 3(a1)]. This is a direct consequence of the absence of topological protection in trivial lattices. In contrast, in the presence of a nontrivial flux [see Fig. 3(a2)] the light remains trapped to the first unit cell, oscillating locally due to the simultaneous excitation of the three edge modes shown in Fig. 1(d), right. We plot the center of mass in Fig. 3(a3) as a function of wavelength, with a shaded area showing the second moment as an indicator of the dispersion. We observe that the light escapes away from the edge and disperses strongly for a trivial lattice (black data). In the topological case (red data), the light oscillates within the first unit cell, with minimal dispersion and a clear revival around 720 nm. While the tuning condition was optimized at around 640 nm, our results show that the destructive interference condition at $\Phi = \pi$ is valid even beyond the tuning zero regime. Nevertheless, we stop measuring at 750 nm to avoid next-nearest-neighbor effects.
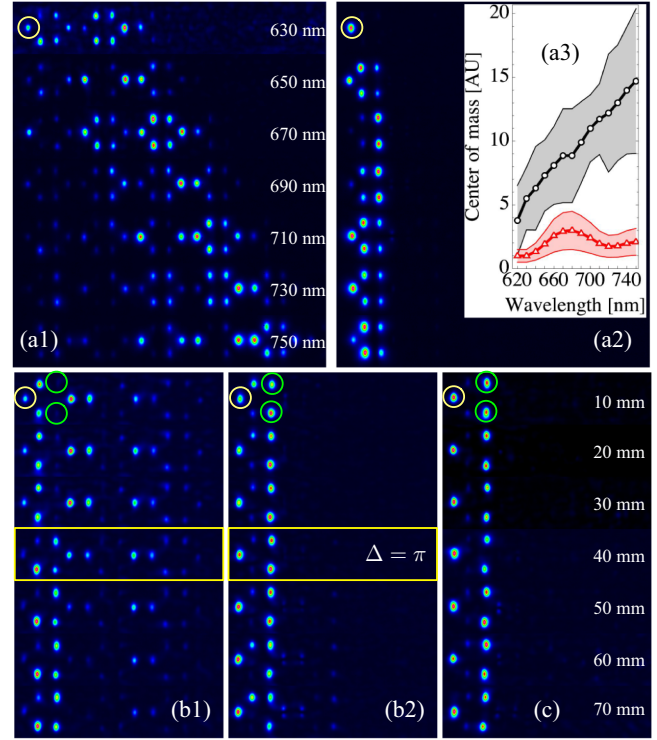

FIG. 3. (a1) and (a2) Output intensities for an A edge site excitation of S and SP lattices, respectively, for the same wavelengths as Figs. 2(d1) and 2(d2). (a3) Center of mass versus wavelength for S (black) and SP (red) lattices, with a shaded area showing the second moment. (b) SLM edge excitation: (b1) and (b2) sweep of the relative input phase Δ in between site A (yellow) and sites C, E (green). Vertical images show different input phases around $\Delta = \pi$ (yellow frame). (c) Excitation of the edge compact topological state at $\Delta = \pi$ versus propagation distance z_s (indicated to the right).

We further investigate the robustness of the compact zero-edge modes. We use an image generator setup [27] to simultaneously excite different lattice sites with a given amplitude and phase structure. We generate a three-site input state at 640 nm and excite sites A, C, and E at the left edge. As shown by yellow and green circles in Fig. 3(b), C and E are excited in phase, while the relative phase (Δ) in A is varied around π. Results for a trivial lattice in Fig. 3(b1) show clear signatures of dispersion and FB oscillations without a tendency for edge localization. On the other hand, for $\Phi = \pi$ we observe in Fig. 3(b2) that the light gets trapped at the first unit cell with almost no dispersion to the lattice bulk. The localization is maintained regardless of the phase structure of the input condition, showing the robustness of the compact edge modes to input phase deviations. This is particularly important in applications in which the phase of an excitation beam is subject to random fluctuations.

Finally, we study the compact edge mode propagation stability and robustness considering fabrication errors. We fix the input phase to $\Delta = \pi$ and fabricate a z-scan

configuration [30], in which the excited sites A, C, and E (at the first unit cell) have a full propagation length, while the rest of the lattice sites have a shorter length z_s. To follow the state evolution, we fabricate 14 lattices with different z_s and show a set of output profiles in Fig. 3(c). We observe an excellent propagation stability of the compact edge mode. As each lattice is fabricated independently, a random fabrication disorder is always present at every sample. Thus, we observe that the zero-edge mode is quite resistant to small deviations of the lattice structure.

In conclusion, we have studied the generation of highly robust topologically protected compact edge modes and, also, we have established a novel procedure for the assessment of topological nontriviality via the mean chiral displacement. Demonstration of the stable compact edge modes is, for example, a decisive stepping stone towards unidirectional topological insulators. Further upgrades, including non-Hermitian Hamiltonians to achieve unidirectional mode propagation or the inclusion of higher dimensions, could make the topological photonic lattices a faithful platform for studying ultralow energy electronics or photonics computing. The experimental implementation of synthetic fluxes and the corresponding MCD estimation open the door to the detection of topological nontriviality in multiband dispersionless systems. We observe the AB caging effect for a very broad wavelength range, showing its strong potential for broadband optical computing. Different geometries [39] or broader sets of effective magnetic fluxes [40,41] are certainly an experimental challenge which could guide further research.

[1] M. Mandal, N. C. Drucker, P. Siriviboon, T. Nguyen, A. Boonkird, T. N. Lamichhane, R. Okabe, A. Chotrattanapituk, and M. Li, Topological superconductors from a materials perspective, Chem. Mater. **35**, 6184 (2023).

[2] G. Liu, S. Lu, Y. Gao, F. Wang, B. Jia, X. Guan, L. H. Han, P. Lu, and H. Song, Band structure optimization of superconducting photonic crystals based on transmission spectrum calculation, Opt. Express **31**, 41905 (2023).

[3] T. Ozawa, R. El-Ganainy, and A. Amo, Photonic topological materials: Feature introduction, Opt. Mater. Express **11**, 1592 (2021).

[4] A. Khanikaev, S. Hossein Mousavi, WK. Tse, M. Kargarian, A. H. MacDonald, and G. Shvets, Photonic topological insulators, Nat. Mater. **12**, 233 (2013).

[5] H. Price *et al.*, Roadmap on topological photonics, J. Phys. Photonics **4**, 032501 (2022).

[6] T. T. Heikkilä and G. E. Volovik, Flat bands as a route to high-temperature superconductivity in graphite, in *Basic Physics of Functionalized Graphite. Springer Series in Materials Science* (Springer, Cham, 2016), pp. 123–143.

[7] M. Tovmasyan, S. Peotta, P. Törmä, and S. D. Huber, Effective theory and emergent SU(2) symmetry in the flat bands of attractive Hubbard models, Phys. Rev. B **94**, 245149 (2016).

[8] V. A. J. Pyykkönen, S. Peotta, and P. Törmä, Suppression of nonequilibrium quasiparticle transport in flat-band superconductors, Phys. Rev. Lett. **130**, 216003 (2023).

[9] P. Törmä, Essay: Where can quantum geometry lead us?, Phys. Rev. Lett. **131**, 240001 (2023).

[10] J. S. Hofmann, F. F. Assaad, and A. P. Schnyder, Edge instabilities of topological superconductors, Phys. Rev. B **93**, 201116(R) (2016).

[11] M. Tovmasyan, S. Peotta, L. Liang, P. Törmä, and S. D. Huber, Preformed pairs in flat Bloch bands, Phys. Rev. B **98**, 134513 (2018).

[12] J. Zurita, C. Creffield, and G. Platero, Tunable zero modes and quantum interferences in flat-band topological insulators, Quantum **5**, 591 (2021).

[13] J. Zurita, C. Creffield, and G. Platero, Topology and interactions in the photonic Creutz and Creutz-Hubbard ladders, Adv. Quantum Technol. **3**, 1900105 (2020).

[14] G. Cáceres-Aravena, L. E. F. Foa Torres, and R. A. Vicencio, Topological and flat-band states induced by hybridized linear interactions in one-dimensional photonic lattices, Phys. Rev. A **102**, 023505 (2020).

[15] M. Mazanov, D. Román-Cortés, G. Cáceres-Aravena, C. Cid, M. Gorlach, and R. A. Vicencio, Photonic molecule approach to multiorbital topology, Nano Lett. **24**, 4595 (2024).

[16] C.-S.Lee, I.-F. Io, and H.-C. Kao, Winding number and Zak phase in multi-band SSH models, Chin. J. Phys. **78**, 96 (2022).

[17] J. K. Asbóth, L. Oroszlány, and A. Pályi, *A Short Course on Topological Insulators* (Springer, Berlin, 2016).

[18] C. Cantillano, S. Mukherjee, L. Morales-Inostroza, B. Real, G. Cáceres-Aravena, C. Hermann-Avigliano, R. R. Thomson, and R. A. Vicencio, Observation of localized ground and excited orbitals in graphene photonic ribbons, New J. Phys. **20**, 033028 (2018).

[19] F. Cardano, A. D'Errico, A. Dauphin *et al.*, Detection of Zak phases and topological invariants in a chiral quantum walk of twisted photons, Nat. Commun. **8**, 15516 (2017).

[20] M. Maffei, A. Dauphin, F. Cardano, M. Lewenstein, and P. Massignan, Topological characterization of chiral models through their long time dynamics, New J. Phys. **20**, 013023 (2018).

[21] A. D'Errico, F. Di Colandrea, R. Barboza, A. Dauphin, M. Lewenstein, P. Massignan, L. Marrucci, and F. Cardano, Bulk detection of time-dependent topological transitions in quenched chiral models, Phys. Rev. Res. **2**, 023119 (2020).

[22] D. Vanderbilt, *Berry Phases in Electronic Structure Theory: Electric Polarization, Orbital Magnetization and Topological Insulators* (Cambridge University Press, Cambridge, England, 2018).

[23] D. Leykam and D. A. Smirnova, Probing bulk topological invariants using leaky photonic lattices, Nat. Phys. **17,** 632 (2021).

[24] A. Szameit, D. Blömer, J. Burghoff, T. Schreiber, T. Pertsch, S. Nolte, A. Tünnermann, and F. Lederer, Discrete nonlinear localization in femtosecond laser written waveguides in fused silica, Opt. Express **13,** 10552 (2005).

[25] C. Jürß and D. Bauer, High-order harmonic generation in hexagonal nanoribbons, Eur. Phys. J. Spec. Top. **230,** 4081 (2021).

[26] H. Drüeke and D. Bauerb, High-harmonic spectra of hexagonal nanoribbons from real-space time-dependent Schrödinger calculations, Eur. Phys. J. Spec. Top. **230,** 4065 (2021).

[27] See Supplemental Material at http://link.aps.org/supplemental/10.1103/PhysRevLett.133.116304 for more details, which includes Ref. [28].

[28] Ch.-K. Chiu, H. Yao, and Sh. Ryu, Classification of topological insulators and superconductors in the presence of reflection symmetry, Phys. Rev. B **88,** 075142 (2013).

[29] P. Delplace, D. Ullmo, and G. Montambaux, Zak phase and the existence of edge states in graphene, Phys. Rev. B **84,** 195452 (2011).

[30] G. Cáceres-Aravena, D. Guzmán-Silva, I. Salinas, and R. A. Vicencio, Controlled transport based on multiorbital Aharonov-Bohm photonic caging, Phys. Rev. Lett. **128,** 256602 (2022).

[31] R. A. Vicencio, Photonic flat band dynamics, Adv. Phys. **6,** 1878057 (2021).

[32] D. Leykam and D. A. Smirnova, Photonic quantum Hall effect, in *Encyclopedia of Condensed Matter Physics (Second Edition)* (Academic Press, New York, 2024), pp. 575–586.

[33] L. Lu, J. D. Joannopoulos, and M. Soljačić, Topological photonics, Nat. Photonics **8,** 821 (2014).

[34] T. Ozawa, H. M. Price, A. Amo, N. Goldman, M. Hafezi, L. Lu, M. C. Rechtsman, D. Schuster, J. Simon, O. Zilberberg, and I. Carusotto, Topological photonics, Rev. Mod. Phys. **91,** 015006 (2019).

[35] S. Longhi, Probing one-dimensional topological phases in waveguide lattices with broken chiral symmetry, Opt. Lett. **43,** 4639 (2018).

[36] Z.-Q. Jiao, S. Longhi, X.-W. Wang, J. Gao, W.-H. Zhou, Y. Wang, Y.-X. Fu, L. Wang, R.-J. Ren, L.-F. Qiao, and X.-M. Jin, Experimentally detecting quantized Zak phases without chiral symmetry in photonic lattices, Phys. Rev. Lett. **127,** 147401 (2021).

[37] G. Cáceres-Aravena, B. Real, D. Guzmán-Silva, P. Vildoso, I. Salinas, A. Amo, T. Ozawa, and R. A. Vicencio, Edge-to-edge topological spectral transfer in diamond photonic lattices, APL Photonics **8,** 080801 (2023).

[38] D. Guzmán-Silva, G. Cáceres-Aravena, and R. A. Vicencio, Experimental observation of interorbital coupling, Phys. Rev. Lett. **127,** 066601 (2021).

[39] S.-R. Eric Yang, M.-C. Cha, H. J. Lee, and Y. H. Kim, Topologically ordered zigzag nanoribbon: $e/2$ fractional edge charge, spin-charge separation, and ground-state degeneracy, Phys. Rev. Res. **2,** 033109 (2020).

[40] S. Mukherjee, M. Di Liberto, P. Öhberg, R. R. Thomson, and N. Goldman, Experimental observation of Aharonov-Bohm cages in photonic lattices, Phys. Rev. Lett. **121,** 075502 (2018).

[41] E. Nicolau, A. M. Marques, R. G. Dias, J. Mompart, and V. Ahufinger, Many-body Aharonov-Bohm caging in a lattice of rings, Phys. Rev. A **107,** 023305 (2023).